

Learning Object Compliance via Young’s Modulus from Single Grasps with Camera-Based Tactile Sensors

Michael Burgess

Department of Mechanical Engineering
Massachusetts Institute of Technology (MIT), United States
mburgjr@mit.edu

Abstract:

Compliance is a useful parametrization of tactile information that humans often utilize in manipulation tasks. It can be used to inform low-level contact-rich actions or characterize objects at a high-level. In robotic manipulation, existing approaches to estimate compliance have struggled to generalize across object shape and material. Using camera-based tactile sensors, we present a novel approach to parametrize compliance through Young’s modulus E . We evaluate our method over a novel dataset of 285 common objects, including a wide array of shapes and materials with Young’s moduli ranging from 5.0 kPa to 250 GPa. Data is collected over automated parallel grasps of each object. Combining analytical and data-driven approaches, we develop a hybrid system using a multi-tower neural network to analyze a sequence of tactile images from grasping. This system is shown to estimate the Young’s modulus of unseen objects within an order of magnitude at 74.2% accuracy across our dataset. This is a drastic improvement over a purely analytical baseline, which exhibits only 28.9% accuracy. Importantly, this estimation system performs irrespective of object geometry and demonstrates robustness across object materials. Thus, it could be applied in a general robotic manipulation setting to characterize unknown objects and inform decision-making, for instance to sort produce by ripeness.

Keywords: Robotic Manipulation, Tactile Sensing, Compliance

1 Introduction

Humans use tactile information to characterize and interact with objects [1]. Through touch, we sense dynamic properties such as friction and compliance [2]. In the case of compliance, we detect discrepancies between soft and hard objects through fingertip pressure and deformation [3].

Compliance has been established as a useful parameter in robotics to classify objects and inform safe grasping policies [4]. It can be directly utilized for a wide variety of biomedical applications [5, 6, 7] or sorting produce by ripeness [8, 9, 10]. Compliance has also been shown to be useful for manipulation through haptic teleoperation systems [11]. Moreover, a reliable measure of compliance could greatly benefit an intelligent, LLM-backed planning architecture [12, 13].

Tactile sensors deployed on robotic end-effectors offer a similar capability to detect dynamic properties as human fingers [14]. High-resolution, camera-based tactile sensors like GelSight have demonstrated strong performance in perceiving properties such as friction and compliance [15, 16]. Incorporating these sensors into robotic systems has proven to be beneficial for executing dynamic tasks [17, 18], including manipulating deformable objects such as cloth or cables [19, 20].

Even with the help of high-resolution tactile sensing, compliance is particularly difficult to discern in unstructured environments. An object’s deformation in response to loading depends both on the object’s shape and its compliance. Without known geometry and pose tracking, analytical methods cannot be utilized to rigorously determine compliance. Instead, learning-based implementations

have been developed to estimate compliance independent of shape [16, 6, 12, 13]. These methods demonstrate relative success in estimating compliance across geometries. However, there remains a challenge of universally describing compliance for all material types.

To better generalize across both shapes and materials, we present a novel compliance estimation system which incorporates analytical modeling alongside learning. Specifically, we use a neural network to combine CNN encoded tactile images with estimates produced by analytical contact models. This hybrid approach allows us to better generalize across materials given an analytical backbone while using learning techniques to account for complex geometries. We validate our approach with a novel dataset of 285 common objects which includes a wide variety of shapes and materials. Our estimation system is shown to perform well across this large, diverse dataset.

Young’s modulus E is a property that defines a material’s resistance to deformation in the elastic regime [21]. We choose to parametrize compliance using Young’s modulus because it is universally defined for all materials and is commonly utilized in well-established mechanical models. For these reasons, it is a natural choice for quantifying compliance in robotic manipulation.

Given an increased ability to generalize across object shape and material type, our compliance estimation architecture could be applied in general robotic manipulation scenarios to characterize unknown objects. More acutely, it could be applied to tasks such as produce sorting to identify ripeness of fruits and vegetables [13, 8, 10].

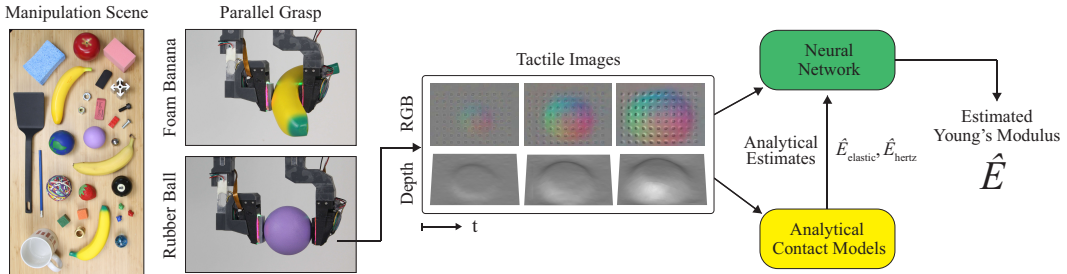


Figure 1: **Young’s modulus estimation system.** Tactile images from parallel grasps of various objects are fed into learned models alongside analytical estimates to generate a hybrid estimate of Young’s modulus. Tactile images are size 35mm by 25mm.

2 Related Work

2.1 GelSight Sensors & Contact Modeling

Camera-based tactile sensors, such as GelSight sensors, are designed to track contact geometry in high-resolution using a camera placed behind an elastomer gel pad [15, 22, 23, 24, 25, 26]. They are highly effective in texture recognition [27, 28, 29], shape and pose estimation [30, 31], and measuring contact force [15] and friction [32]. However, reliably modeling contact with these soft sensors remains challenging. Simulators have been developed to generate tactile images and deformed geometry of sensors using pre-computed finite element method (FEM) solutions [33]. Finite element analysis has proven a viable way to model soft contact on hardware and used to estimate forces from tactile data [34, 35]. Though modeling with FEM is accurate, it requires a precise map of object geometry and solutions must be pre-computed offline.

Alternative approaches have been developed using Hertzian mechanics to model soft contact in robotic grasping [36, 37]. This closed-form method offers improved computational efficiency over FEM and simulated methods. Still, it requires assumptions on contact geometry, namely that geometry should be axisymmetric. Hertzian contact models have been utilized for force estimation [38, 6] and surface curvature detection from tactile data [39]. Since they are closed-form, these constitutive models can more easily be inverted to determine object compliance.

2.2 Compliance Estimation

Estimating the compliance of a contacted object remains a complex problem in robotic manipulation, particularly without assumptions on object shape or material type. Analytical approaches to compliance estimation often lack robustness to variations in geometry. A traditional approach to model compliance is to apply Hooke’s Law using measurements of grasping force and positions [4]. Similar models have been foundational in developing low-level grasping control policies [40, 41]. This method can provide an effective stiffness of grasping. However, it requires assumptions on object shapes and may struggle when handling complex geometries without a known map of each grasped object. By incorporating tactile sensing, it is possible to create higher fidelity compliance estimation models [42, 43, 44]. These methods have a stronger ability to sense and generalize across contact geometry but still struggle to account for complex contact geometries.

Recent learning-based approaches to compliance estimation have demonstrated the ability to generalize across geometry but struggle across a wide-range of material types. Work has been done to create a tactile-informed model to estimate the Shore 00 hardness of an object in contact with a GelSight sensor. The architecture predicts hardness directly from tactile images without any mechanical modeling [45, 16]. Shore 00 hardness is a measure designed to quantify the compliance of soft rubbers [46]. Thus, this method is trained using only rubber objects. It is fundamentally restricted to predicting on this scale and cannot express differences in compliance between more rigid objects. LLM-backed methods have been developed to classify tactile images with binary semantic descriptions of ‘soft’ or ‘hard’ [12, 13]. These large-data methods are promising but still have not been used to assess compliance on a continuous scale across material types. Other data-driven implementations have been developed using tactile sensing to directly measure the ripeness of produce [8, 9, 10]. As before, these methods are restricted by their dataset and labeling method. In all cases, labeling choices prevent models from incorporating analytical modeling alongside learning.

3 Methods

3.1 Overview

We develop a hybrid system fusing analytical models alongside learning to estimate the Young’s modulus of general unknown objects from a single parallel grasp. Through analytical modeling, we can create a well-founded, preliminary estimate for Young’s modulus. By incorporating learning, we can compensate for assumptions taken by analytical models to better generalize across contact geometry. A large, diverse dataset of 285 common objects is collected to train and evaluate our method. Our approach of combining analytical models with data-driven methods is partially inspired by residual physics architectures [47] and physics-informed tactile models [48].

Our hybrid estimation architecture is displayed in Fig. 2. Tactile images and measurements of force F and gripper width w are fed into Hertzian and elastic analytical models to fit respective estimates of Young’s modulus $\hat{E}_{\text{elastic}}, \hat{E}_{\text{hertz}}$. In parallel, a selected number N_{frames} of tactile images are fed into a data-driven model. Features extracted from images are concatenated with grasp measurements into a large fully-connected decoder. This multi-tower architecture is similar to other grasp-based learning architectures [49]. Output features from our learned model are sent to a smaller decoder alongside analytical estimates to produce a final hybrid estimate of Young’s modulus \hat{E} .

Code for the project is publicly available on GitHub. Collected data for multiple grasps of all objects with labeled Young’s moduli and Shore hardness is publicly available on HuggingFace.

3.2 Analytical Contact Models

Simple Elasticity Parallel grasping can be modeled as uniaxial loading using an adaptation of Hooke’s Law. A diagram of parallel grasping is provided in Fig. 3. At every instance t , force F is applied to the grasped object, with gripper at width w . Traditional methods have used these measurements alone to estimate the compliance or stiffness of grasped objects [4].

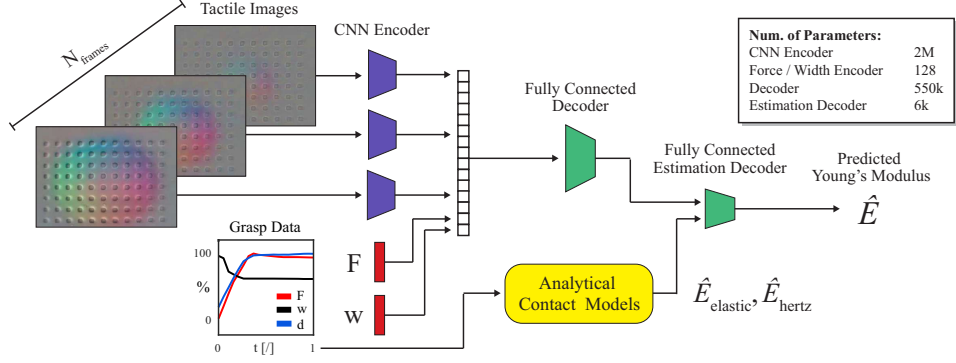


Figure 2: **Young’s modulus estimation architecture.** Tactile images, depth, and measured grasping force F and width w are sent into analytical and learned models. Estimates from analytical models are fed into a fully-connected decoder alongside learned grasp features.

With camera-based tactile sensing, we can increase the fidelity of the model by measuring contact area A and depth d [15]. Contact area A is determined by masking depth images with constant threshold of 0.1mm. This threshold was chosen empirically to cancel out potential noise. Without tactile sensing, we could not measure depth ($d(t) = 0$) and would need to assume constant contact area ($A(t) = A_{\text{sensor}}$). We use measurements to calculate contact stress σ and object strain ϵ , following Eq. 1. We define $t = 0$ to be the moment of first contact, where $F(t = 0)$ must be greater than an empirically-defined threshold.

$$\sigma(t) = \frac{F(t)}{A(t)}, \quad \epsilon(t) = \frac{\Delta w(t) + 2\Delta d(t)}{w(0) + 2d(0)} = \frac{(w(t) + 2d(t)) - (w(0) + 2d(0))}{w(0) + 2d(0)} \quad (1)$$

In the elastic regime, stress σ and ϵ are related by Young’s modulus [21]. Using measurements across grasping time t , we fit an estimate for Young’s modulus \hat{E}_{elastic} following Eq. 2.

$$\sigma = \hat{E}_{\text{elastic}} \epsilon \quad (2)$$

Despite its simplicity, this method does not properly consider the geometry of unknown objects. It implicitly assumes objects have a consistent profile along the grasping axis. Furthermore, it does not take advantage of precise information about the deformation of contact geometry that is apparent through high-resolution tactile data.

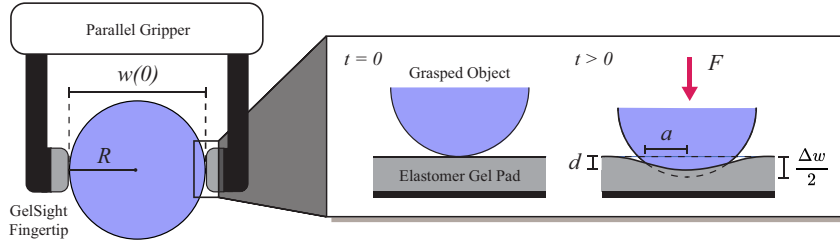


Figure 3: **Simple mechanics of parallel grasping.** Spherical object of radius R is grasped with soft GelSight sensors. Normal force F is applied at width w . Penetration depth d and contact radius a can be measured with tactile sensors. Timestep $t = 0$ is the moment of first contact over the grasp.

Hertzian Contact Hertzian contact theory examines the deformation of elastic bodies through contact [50]. In a simple case, contact is assumed to be without friction or adhesion [51, 52]. Unlike the previously-described method, Hertzian mechanics more acutely analyzes geometry through contact. It has been used to model soft contact in robotics [36, 39], including GelSight-like tactile sensors [23, 6]. Precise depth sensing allows us to track surface deformation and apply this model.

GelSight sensors are made with highly elastic silicone rubber [22]. Unless the grasped object is fully rigid, we expect both bodies to deform through contact. This implies the maximum measured penetration depth d will be less than the relative displacement between the finger and object $d < \frac{\Delta w}{2}$.

This phenomenon is depicted in Fig. 3. An aggregate modulus E^* describes the bodies’ combined resistance to deformation in Eq. 3, which depends on the Poisson’s ratio ν of each body.

$$\frac{1}{E^*} = \frac{1 - \nu_{\text{sensor}}^2}{E_{\text{sensor}}} + \frac{1 - \nu_{\text{obj}}^2}{E_{\text{obj}}} \quad (3)$$

Hertzian solutions have been derived for a wide range of contact geometries [53]. Since we are analyzing contact with an unknown object whose shape is not precisely known, we model all contact geometry as spherical. This is a reasonable simplification for convex objects, but may produce bounded errors in estimates over our geometrically diverse dataset. Our neural network will learn to compensate for this intrinsic and repeatable geometric modeling error.

Since we assume contact profiles are spherical, we must calculate contact radius a . This is the radius needed for a circle’s contact area to match the observed contact area A . Additionally, we can approximate the apparent radius of the unknown object R through observed contact area and gripper displacement [53]. Using these parameters and the method of dimensionality reduction (MDR), we can calculate the sensor’s surface deformation in response to elastic loading [53, 54]. This relates force F and depth d by E^* . This relation shows that a harder sphere will plunge deeper into the contact plane, assuming constant force. More detailed derivation for this expression and discussion about the MDR is provided in Appendix A.

$$a(t) = \sqrt{\frac{A(t)}{\pi}}, \quad R(t) = \frac{a^2(t)}{\Delta w(t)}, \quad d(t) = \frac{1 - \nu_{\text{sensor}}^2}{E_{\text{sensor}}} \left(\frac{3E^{*2}F(t)}{32R^2(t)} \right)^{\frac{1}{3}} a(t) \quad (4)$$

With measured data over the duration of a grasp, we apply least-squares to retrieve a best fit value \hat{E}^* . Then, we use \hat{E}^* to compute an estimated modulus for our unknown object \hat{E}_{hertz} , given known properties of our sensor $E_{\text{sensor}} = 0.275$ MPa, $\nu_{\text{sensor}} = 0.48$. We assume constant $\nu_{\text{obj}} = 0.4$ based on the Poisson’s ratio of common materials [55]. After analytical estimates are computed, linear scaling is added to account for potential constant errors across the dataset.

$$\hat{E}_{\text{hertz}} = (1 - \nu_{\text{obj}}^2) \left(\frac{1}{\hat{E}^*} - \frac{1 - \nu_{\text{sensor}}^2}{E_{\text{sensor}}} \right)^{-1} \quad (5)$$

4 Physical Dataset

A novel physical dataset of 285 objects was gathered to train and validate our method. For comparison, our dataset is nearly 4 times larger than the YCB dataset, which includes only 77 objects [56]. Chosen objects were intended to be among things a robotic manipulator may commonly interact with in general operation. Additionally, each object was required to have approximately uniform material composition to ensure that an accurate Young’s modulus could be defined for the object and used to label data for supervised training. A subset of dataset objects is displayed in Fig. 4.

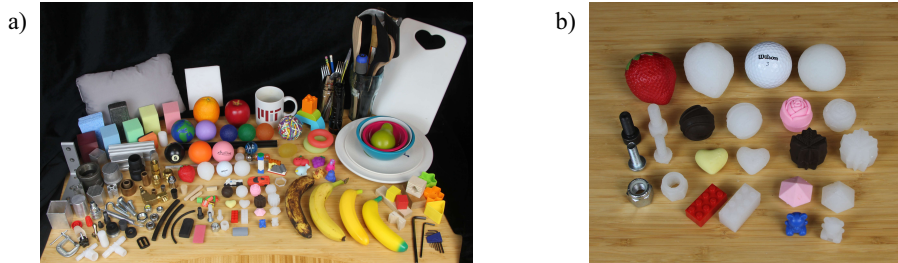


Figure 4: **Physical dataset.** (a) Selected objects from our physical dataset are displayed. These are common objects with a wide variety of shapes and materials. (b) Some custom objects are molded out of silicone to replicate the shape of non-rubber objects in the dataset.

To evaluate how well estimation algorithms could generalize, diversity of shape and material was prioritized in acquiring objects. Thus, we mold 20 custom objects out of silicone to replicate the exact shape of other objects in the dataset with vastly different material composition. Molded objects

are displayed in Fig. 4b. Training on data collected across object replicas of different materials will help prevent overfitting to shapes and textures. Moreover, there is incentive to bias towards rubber objects because it is clear from Eq. 5 that it will be easiest to discriminate between Young’s moduli nearest to our sensor’s. The dataset’s composition is further detailed in Appendix D.

As objects were gathered, they were labeled with their Young’s moduli. For harder objects, like those made of metals and plastics, this was done by referencing an engineering database of material properties [57], as all objects are made of known materials. For softer objects, like those made of rubber, Shore hardness was measured and converted to Young’s modulus. Shore hardness is converted to Young’s modulus using Gent’s model of hardness and other established methods [46, 58]. These models provide a reliable measure of object compliance on a logarithmic scale. The dataset includes materials ranging from foam to steel, with Young’s moduli from 5.0 kPa to 250 GPa. For reference, our sensor’s Young’s modulus is 0.275 MPa.

5 Experiments

5.1 Hardware Setup

GelSight Wedge sensors [22] were rigidly attached to a standard parallel robotic gripper with 3D-printed plastic fingers, as depicted in Fig. 5. One sensor is inscribed with markers for tracking surface displacement. Markers help provide information about shear forces and surface displacement, as further explained in Appendix B. By collecting data with different sensors simultaneously, we have the ability to assess the relative necessity of markers in estimating Young’s modulus. Normal force is measured through a gauge embedded in the left finger. Gripper position is directly measured from control software.

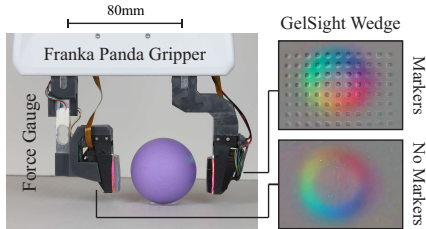


Figure 5: **Hardware setup for data collection.** GelSight Wedge sensors are attached to Franka Panda gripper with embedded force gauge.

5.2 Data Collection & Training

Data Collection: Automated parallel grasps are executed on objects in fixed position. For each object in our dataset, a set number of grasps are recorded. Objects are re-oriented between each grasp to diversify potential antipodal grasp locations. During grasping, tactile images from GelSight sensors, forces, and gripper widths, are recorded at 30 Hz. Measurements are synchronized by shifting for latency between cameras. Grasps are executed at constant velocity up to force of 30 N. Raw data collected from grasps of spherical objects is plotted in Fig. 6. More details about processing data collected from grasps is provided in Appendix C.

Tactile and depth images at grasping force of 30 N for a set of example objects are depicted in Fig. 7. We observe that textures are more finely captured for rigid object’s with higher modulus. As expected by Eq. 4, peak depth is higher for objects of the same shape with higher modulus.

Data Preprocessing: Data recorded from grasping objects is clipped to include only the loading sequence from first contact to peak force. Misaligned grasps where loading is non-monotonic are disregarded. From here, a set number of frames $N_{\text{frames}} = 3$ are sampled equidistantly in time. Multiple augmentations of samples are taken from each grasp. As depicted in Fig. 2, tactile images are sent as inputs to our multi-tower architecture alongside analytical estimates and force and width measurements. Images are randomly transformed with horizontal and vertical flipping.

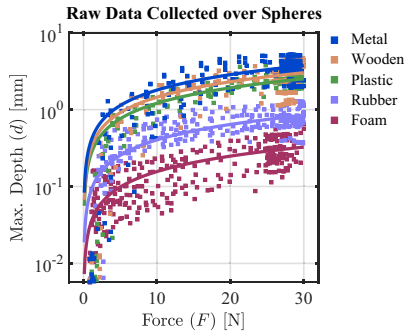


Figure 6: **Raw force and depth data.** Data is collected across grasps for spheres of each material type. Data is fit to functions of the form $d \sim F^{\frac{2}{3}}$, per our Hertzian model.

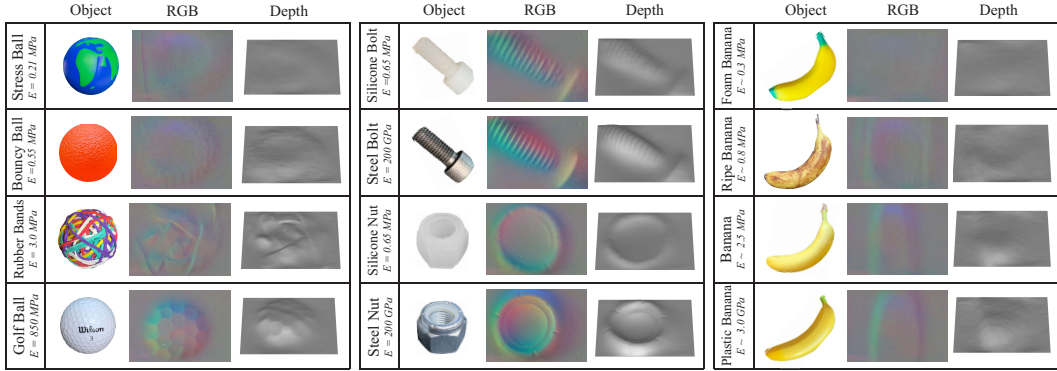


Figure 7: **Example tactile data.** Tactile images and depth reconstruction from a GelSight Wedge sensor without markers over a set of example objects. Shown frames are all from peak pressing force of 30 N. Tactile images are size 35mm by 25mm.

Training: We train our model for 80 iterations over 4,000 grasp inputs. In total, these grasps include more than 12,000 tactile images. Output labels are normalized on a log10 scale given the range of Young’s moduli in our dataset. Final sigmoid activation function is used with an MSE loss function.

6 Experimental Results

We train our neural network with preprocessed data as described in Section 5.2. Initially, we train a model over only rubber objects. This preliminary exercise is performed to evaluate the model’s ability to learn across a constrained dataset. Rubber objects are closest to the Young’s modulus of our sensor. From Eq. 5, we expect it will be easier to discern finer differences in compliance between them. Results over unseen objects for this model are plotted in Fig. 8. The model demonstrates 100% prediction accuracy within an order of magnitude of the ground truth Young’s modulus. The prediction range of this experiment is analogous to previously developed Shore hardness tactile models [16], which are designed to estimate the compliance of soft rubber objects. Shore 00 hardness values evaluated in [16] range from approximately 6 kPa to 2 MPa. Here, we include harder rubber objects as well.

We train our neural network over the entire collected dataset. This learned model is compared to analytical baselines. Predictions across the dataset for each method are plotted in Fig. 9. We observe that as the traditional Hooke’s Law method without tactile sensing fails to distinguish between all material types. Simple elastic and Hertzian analytical methods demonstrate significant improvements, but are still less than 30% accurate. Our learned model showcases dramatic improvements over all other methods.

All estimation methods had more difficulty expressing precise differences in Young’s modulus between harder objects that strayed further from the modulus of the sensor (i.e. plastic, wood, and metal objects). Additionally, we observe decreased overall accuracy from previous evaluation over the rubber subset of our dataset. These results are expected given that harder objects are approximately rigid relative to the soft sensor’s Young’s modulus. The resolution of the tactile sensor is likely not high enough to detect small differences in deformation between this range of compliances.

In Table 1, performance is compared between different estimation methods and inputs. Performance metrics are computed for grasps of both seen and unseen objects. We evaluate models on a logarithmic scale given the range of Young’s moduli in our dataset. Predictions are considered sufficiently

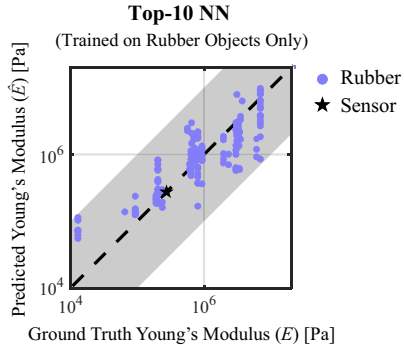


Figure 8: **Young’s modulus predictions for rubber objects only.** Results for model trained on only rubber objects over 80 randomly sampled grasps of unseen objects. Predictions in the gray region are considered sufficiently accurate.

accurate within the same order of magnitude of ground truth labels. We compute error as the average difference between prediction and ground truth on a log10 scale.

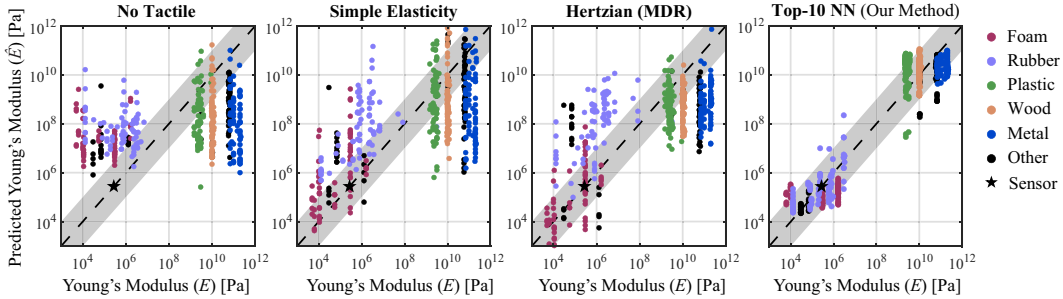


Figure 9: **Young’s modulus predictions by material.** Results for learned and analytical estimation methods are plotted, using predictions from 80 randomly sampled grasps per material category. Predictions in the gray region are considered sufficiently accurate.

From the ablation study, we observe that our learned model vastly reduces error and improves accuracy over analytical methods. Furthermore, we see that RGB tactile images with markers are favorable for this estimation task. However, we do not observe significant difference in results between models which consider force F and width w measurements. This may be due to the fact that all objects were grasped with nearly identical peak force. Moreover, force is implicitly detectable through tactile images [16]. Importantly, considering analytical estimates \hat{E}_{elastic} , \hat{E}_{hertz} is shown to improve learned prediction results. This demonstrates that incorporating analytical modeling improves our ability to discern compliance over a purely learning-based method. Accuracy and error metrics are computed across shape and material categories for each method in Appendix D. We observe that our model performs independent of shape and can generalize well across materials.

Method	Inputs					Seen Objects		Unseen Objects	
	Depth / RGB	Markers	F	w	$\hat{E}_{\text{elastic}}, \hat{E}_{\text{hertz}}$	Log10 Error	Log10 Acc.	Log10 Error	Log10 Acc.
No Tactile	—	—	✓	✓	—	—	—	2.13	18.2%
Simple Elasticity	Depth	—	✓	✓	—	—	—	1.90	27.3%
Hertzian (MDR)	Depth	—	✓	✓	—	—	—	1.68	28.9%
Top-10 NN (Our Method)	RGB	✓	✓	✓	✓	0.73	76.9%	0.76	73.5%
	RGB	✓	×	×	✓	0.73	78.5%	0.76	74.2%
	RGB	×	✓	✓	✓	0.85	70.4%	0.88	68.6%
	RGB	×	×	×	✓	0.85	69.6%	0.90	67.9%
	RGB	✓	✓	✓	×	0.63	80.4%	0.86	64.6%
	RGB	✓	×	×	×	0.65	78.5%	0.85	65.0%
	Depth	—	✓	✓	✓	1.05	61.7%	0.98	63.6%
Depth	—	×	×	×	1.08	60.1%	1.04	59.4%	

Table 1: Estimation Architecture Ablation Study

7 Conclusion

We have developed a novel system for estimating the Young’s modulus of unknown contacted objects using analytical and data-driven methods. This system can create estimates online from only a single parallel grasp. It has been shown to perform independent of object shape and demonstrates robustness across materials. It can expressively distinguish precise differences in compliance between soft objects. The system is less capable of measuring precise differences between harder, such as plastic and metal, objects which are effectively rigid relative to the soft GelSight sensor.

The estimation system introduced in this paper could be applied for use with other camera-based tactile sensors capable of tracking depth. With more diverse tactile data, the accuracy of the system could be further improved. Given an increased ability to generalize, this compliance estimation system could be deployed alongside an intelligent high-level controller to inform decision-making in robotic manipulation scenarios by characterizing the compliance of unknown objects. As one example, it could be utilized to identify the ripeness of fruits or vegetables [13, 8, 10].

Acknowledgments

The authors would like to thank Sandra Q. Liu, Jialiang (Alan) Zhao, Megha Tippur, Yuxiang Ma, and Laurence Willemet for their guidance and insight provided throughout the project’s duration.

References

- [1] N. Navarro-Guerrero, S. Toprak, J. Josifovski, and L. Jamone. Visuo-haptic object perception for robots: an overview. *Auton. Robots*, 47(4):377–403, Apr. 2023.
- [2] W. M. Bergmann Tiest. Tactual perception of material properties. *Vision Research*, 50(24): 2775–2782, 2010. ISSN 0042-6989. doi:<https://doi.org/10.1016/j.visres.2010.10.005>. URL <https://www.sciencedirect.com/science/article/pii/S0042698910004967>. Perception and Action: Part I.
- [3] M. A. Srinivasan and R. H. LaMotte. Tactual discrimination of softness. *J. Neurophysiol.*, 73 (1):88–101, Jan. 1995.
- [4] M. R. Cutkosky. *Mechanical properties for the grasp of a robotic hand*. Department of Computer Science, Carnegie-Mellon University, 1984.
- [5] M. I. Tiwana, S. J. Redmond, and N. H. Lovell. A review of tactile sensing technologies with applications in biomedical engineering. *Sensors and Actuators A: Physical*, 179:17–31, 2012. ISSN 0924-4247. doi:<https://doi.org/10.1016/j.sna.2012.02.051>. URL <https://www.sciencedirect.com/science/article/pii/S0924424712001641>.
- [6] J. Di, Z. Dugonjic, W. Fu, T. Wu, R. Mercado, K. Sawyer, V. R. Most, G. Kammerer, S. Speidel, R. E. Fan, G. Sonn, M. R. Cutkosky, M. Lambeta, and R. Calandra. Using fiber optic bundles to miniaturize vision-based tactile sensors, 2024.
- [7] S. Sanan, S. Tully, A. Bajo, N. Simaan, and H. Choset. Simultaneous compliance and registration estimation for robotic surgery. In *Robotics: Science and Systems*, 2014.
- [8] L. He, L. Tao, Z. Ma, X. Du, and W. Wan. Cherry tomato firmness detection and prediction using a vision-based tactile sensor. *Journal of Food Measurement and Characterization*, 18(2):1053–1064, Nov. 2023. ISSN 2193-4134. doi:[10.1007/s11694-023-02249-0](https://doi.org/10.1007/s11694-023-02249-0). URL <http://dx.doi.org/10.1007/s11694-023-02249-0>.
- [9] F. E. Erukainure, V. Parque, M. Hassan, and A. M. FathEl-Bab. Estimating the stiffness of kiwifruit based on the fusion of instantaneous tactile sensor data and machine learning schemes. *Computers and Electronics in Agriculture*, 201:107289, 2022. ISSN 0168-1699. doi:<https://doi.org/10.1016/j.compag.2022.107289>. URL <https://www.sciencedirect.com/science/article/pii/S0168169922006019>.
- [10] I. Fahmy, I. Hussain, N. Werghi, T. Hassan, and L. Seneviratne. Hapticformers: Utilizing transformers for avocado maturity grading through vision-based tactile assessment, 02 2024.
- [11] A. Bicchi, E. Scilingo, and D. De Rossi. Haptic discrimination of softness in teleoperation: the role of the contact area spread rate. *IEEE Transactions on Robotics and Automation*, 16 (5):496–504, 2000. doi:[10.1109/70.880800](https://doi.org/10.1109/70.880800).
- [12] L. Fu, G. Datta, H. Huang, W. C.-H. Panitch, J. Drake, J. Ortiz, M. Mukadam, M. Lambeta, R. Calandra, and K. Goldberg. A touch, vision, and language dataset for multimodal alignment, 2024.
- [13] S. Yu, K. Lin, A. Xiao, J. Duan, and H. Soh. Octopi: Object property reasoning with large tactile-language models, 2024.

- [14] S. Luo, J. Bimbo, R. Dahiya, and H. Liu. Robotic tactile perception of object properties: A review. *Mechatronics*, 48:54–67, 2017. ISSN 0957-4158. doi:<https://doi.org/10.1016/j.mechatronics.2017.11.002>. URL <https://www.sciencedirect.com/science/article/pii/S0957415817301575>.
- [15] W. Yuan, S. Dong, and E. H. Adelson. Gelsight: High-resolution robot tactile sensors for estimating geometry and force. *Sensors*, 17(12):2762, 2017.
- [16] W. Yuan, C. Zhu, A. Owens, M. A. Srinivasan, and E. H. Adelson. Shape-independent hardness estimation using deep learning and a gelsight tactile sensor. In *2017 IEEE International Conference on Robotics and Automation (ICRA)*. IEEE, May 2017. doi:[10.1109/icra.2017.7989116](https://doi.org/10.1109/icra.2017.7989116). URL <http://dx.doi.org/10.1109/ICRA.2017.7989116>.
- [17] C. Wang, S. Wang, B. Romero, F. Veiga, and E. Adelson. Swingbot: Learning physical features from in-hand tactile exploration for dynamic swing-up manipulation, 2021.
- [18] K. Ota, D. K. Jha, K. M. Jatavallabhula, A. Kanezaki, and J. B. Tenenbaum. Tactile estimation of extrinsic contact patch for stable placement, 2024.
- [19] Y. She, S. Wang, S. Dong, N. Sunil, A. Rodriguez, and E. Adelson. Cable manipulation with a tactile-reactive gripper. *Int. J. Rob. Res.*, 40(12-14):1385–1401, Dec. 2021.
- [20] N. Sunil, S. Wang, Y. She, E. Adelson, and A. Rodriguez. Visuotactile affordances for cloth manipulation with local control. *arXiv preprint arXiv:2212.05108*, 2022.
- [21] R. C. Hibbeler. *Mechanics of materials*. MacMillan Publishing Company, 1994.
- [22] S. Wang, Y. She, B. Romero, and E. Adelson. Gelsight wedge: Measuring high-resolution 3d contact geometry with a compact robot finger. In *2021 IEEE International Conference on Robotics and Automation (ICRA)*, pages 6468–6475. IEEE, 2021.
- [23] I. H. Taylor, S. Dong, and A. Rodriguez. Gelslim 3.0: High-resolution measurement of shape, force and slip in a compact tactile-sensing finger. In *2022 International Conference on Robotics and Automation (ICRA)*, pages 10781–10787. IEEE, 2022.
- [24] S. Q. Liu and E. H. Adelson. Gelsight fin ray: Incorporating tactile sensing into a soft compliant robotic gripper, 2022.
- [25] M. H. Tippur and E. H. Adelson. Gelsight360: An omnidirectional camera-based tactile sensor for dexterous robotic manipulation, 2023.
- [26] J. Zhao and E. H. Adelson. Gelsight svelte hand: A three-finger, two-dof, tactile-rich, low-cost robot hand for dexterous manipulation. *arXiv preprint arXiv:2309.10886*, 2023.
- [27] R. Li and E. H. Adelson. Sensing and recognizing surface textures using a gelsight sensor. In *Proceedings of the IEEE Conference on Computer Vision and Pattern Recognition (CVPR)*, June 2013.
- [28] S. Luo, W. Yuan, E. Adelson, A. Cohn, and R. Fuentes. Cloth texture recognition using vision and tactile sensing. 05 2018.
- [29] A. Amini, J. I. Lipton, and D. Rus. Uncertainty aware texture classification and mapping using soft tactile sensors. In *2020 IEEE/RSJ International Conference on Intelligent Robots and Systems (IROS)*, pages 4249–4256, 2020. doi:[10.1109/IROS45743.2020.9341045](https://doi.org/10.1109/IROS45743.2020.9341045).
- [30] M. Bauza, O. Canal, and A. Rodriguez. Tactile mapping and localization from high-resolution tactile imprints, 2019.

- [31] J. Zhao, M. Bauza, and E. H. Adelson. Fingerslam: Closed-loop unknown object localization and reconstruction from visuo-tactile feedback, 2023.
- [32] W. Yuan, R. Li, M. A. Srinivasan, and E. H. Adelson. Measurement of shear and slip with a gelsight tactile sensor. In *2015 IEEE International Conference on Robotics and Automation (ICRA)*, pages 304–311, 2015. doi:10.1109/ICRA.2015.7139016.
- [33] Z. Si and W. Yuan. Taxim: An example-based simulation model for gelsight tactile sensors, 2021.
- [34] D. Ma, E. Donlon, S. Dong, and A. Rodriguez. Dense tactile force estimation using gelslim and inverse fem. In *2019 International Conference on Robotics and Automation (ICRA)*, pages 5418–5424, 2019. doi:10.1109/ICRA.2019.8794113.
- [35] I. Taylor, S. Dong, and A. Rodriguez. Gelslim3.0: High-resolution measurement of shape, force and slip in a compact tactile-sensing finger, 2021.
- [36] Y. Li and I. Kao. A review of modeling of soft-contact fingers and stiffness control for dextrous manipulation in robotics. In *Proceedings 2001 ICRA. IEEE International Conference on Robotics and Automation (Cat. No.01CH37164)*, volume 3, pages 3055–3060 vol.3, 2001. doi:10.1109/ROBOT.2001.933086.
- [37] C. J. Stabile, D. J. Levine, G. M. Iyer, C. Majidi, and K. T. Turner. The role of stiffness in versatile robotic grasping. *IEEE Robotics and Automation Letters*, 7(2):4733–4740, 2022. doi:10.1109/LRA.2022.3149036.
- [38] B. W. McInroe, C. L. Chen, K. Y. Goldberg, R. Bajcsy, and R. S. Fearing. Towards a soft fingertip with integrated sensing and actuation. In *2018 IEEE/RSJ International Conference on Intelligent Robots and Systems, IROS 2018, Madrid, Spain, October 1-5, 2018*, pages 6437–6444. IEEE, 2018. doi:10.1109/IROS.2018.8594032. URL <https://doi.org/10.1109/IROS.2018.8594032>.
- [39] X. Lin, L. Willemet, A. Bailleul, and M. Wiertelwski. Curvature sensing with a spherical tactile sensor using the color-interference of a marker array. In *2020 IEEE International Conference on Robotics and Automation (ICRA)*, pages 603–609, 2020. doi:10.1109/ICRA40945.2020.9197050.
- [40] J. K. Salisbury. Active stiffness control of a manipulator in cartesian coordinates. *1980 19th IEEE Conference on Decision and Control including the Symposium on Adaptive Processes*, pages 95–100, 1980. URL <https://api.semanticscholar.org/CorpusID:1758620>.
- [41] K. M. Lynch and F. C. Park. *Modern Robotics: Mechanics, Planning, and Control*. Cambridge University Press, USA, 1st edition, 2017. ISBN 1107156300.
- [42] C. Ciliberto, L. Fiorio, M. Maggiali, L. Natale, L. Rosasco, G. Metta, G. Sandini, and F. Nori. Exploiting global force torque measurements for local compliance estimation in tactile arrays. In *2014 IEEE/RSJ International Conference on Intelligent Robots and Systems*, pages 3994–3999, 2014. doi:10.1109/IROS.2014.6943124.
- [43] G. Kinoshita, Y. Sugeno, H. Oosumi, K. Umeda, and Y. Muranaka. High compliance sensing behavior of a tactile sensor. In *Proceedings 1999 IEEE/RSJ International Conference on Intelligent Robots and Systems. Human and Environment Friendly Robots with High Intelligence and Emotional Quotients (Cat. No.99CH36289)*, volume 2, pages 826–831 vol.2, 1999. doi:10.1109/IROS.1999.812782.
- [44] Z. Su, J. Fishel, T. Yamamoto, and G. Loeb. Use of tactile feedback to control exploratory movements to characterize object compliance. *Frontiers in neurorobotics*, 6:7, 07 2012. doi:10.3389/fnbot.2012.00007.

- [45] W. Yuan, M. A. Srinivasan, and E. H. Adelson. Estimating object hardness with a gelsight touch sensor. In *2016 IEEE/RSJ International Conference on Intelligent Robots and Systems (IROS)*, pages 208–215, 2016. doi:10.1109/IROS.2016.7759057.
- [46] A. N. Gent. On the relation between indentation hardness and young’s modulus. *Rubber Chemistry and Technology*, 31:896–906, 1958. URL <https://api.semanticscholar.org/CorpusID:136730823>.
- [47] A. Zeng, S. Song, J. Lee, A. Rodriguez, and T. Funkhouser. Tossingbot: Learning to throw arbitrary objects with residual physics. 2019.
- [48] H.-J. Huang, X. Guo, and W. Yuan. Understanding dynamic tactile sensing for liquid property estimation, 2022.
- [49] J. Mahler, J. Liang, S. Niyaz, M. Laskey, R. Doan, X. Liu, J. A. Ojea, and K. Goldberg. Dex-net 2.0: Deep learning to plan robust grasps with synthetic point clouds and analytic grasp metrics, 2017.
- [50] H. Hertz. The contact of elastic solids. *J Reine Angew, Math*, 92:156–171, 1881.
- [51] V. L. Popov et al. *Contact mechanics and friction*. Springer, 2010.
- [52] K. L. Johnson. *Contact mechanics*. Cambridge university press, 1987.
- [53] V. L. Popov, M. Heß, and E. Willert. *Handbook of contact mechanics: exact solutions of axisymmetric contact problems*. Springer Nature, 2019.
- [54] W. Zunker and K. Kamrin. A mechanically-derived contact model for adhesive elastic-perfectly plastic particles. part i: Utilizing the method of dimensionality reduction, 2023.
- [55] G. N. Greaves, A. L. Greer, R. S. Lakes, and T. Rouxel. Poisson’s ratio and modern materials. *Nat. Mater.*, 10(11):823–837, Oct. 2011.
- [56] B. Calli, A. Singh, J. Bruce, A. Walsman, K. Konolige, S. Srinivasa, P. Abbeel, and A. M. Dollar. Yale-CMU-Berkeley dataset for robotic manipulation research. *Int. J. Rob. Res.*, 36(3): 261–268, Mar. 2017.
- [57] Material property data. *MatWeb*, 2024. URL <https://www.matweb.com/>.
- [58] K. Larson. Can you estimate modulus from durometer hardness for silicones? yes, but only roughly . . . and you must choose your modulus carefully! *Dow White Paper*, 09 2017.
- [59] V. Popov and M. Heß. Method of dimensionality reduction in contact mechanics and friction: A users handbook. i. axially-symmetric contacts. *Acta Universitatis*, 12:1–14, 04 2014.

A Method of Dimensionality Reduction (MDR)

As discussed in Section 3.2, we model contact between an unknown object and our camera-based tactile sensor as a collision between an elastic sphere and an elastic half-space using Hertzian contact theory. Now, we will walk through the derivation for a constitutive relation using the method of dimensionality reduction (MDR) [59]. A mechanical diagram of contact at time t with labeled variables is provided in Fig. 10.

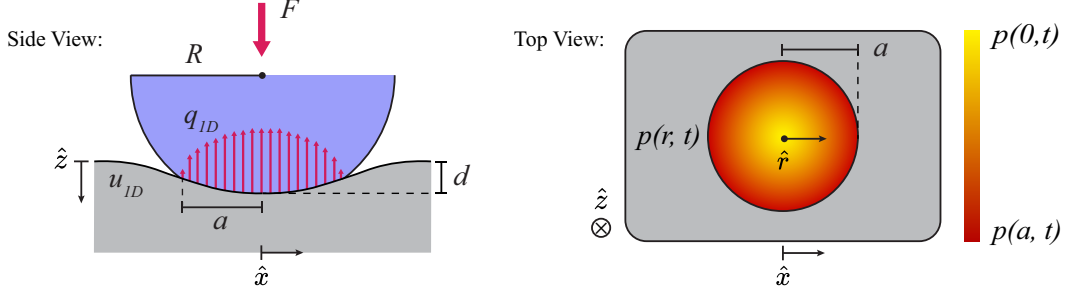


Figure 10: **Method of dimensionality reduction (MDR) diagram.** An elastic sphere is colliding with an elastic half-space at time t . Variables of contact are labeled. The two-dimensional radial stress field p is transformed into a one-dimensional force field q_{1D} . This transformation can be observed through comparison of top and side views.

First, we compute the maximum pressure of contact p_0 between both bodies in Eq. 6. This is a simple expression of measured force F and contact radius a . We can substitute a to create an expression dependent on the aggregate elastic compliance of the bodies E^* [52].

$$p_0(t) = \frac{3F(t)}{2\pi a^2(t)} = \frac{1}{\pi} \left(\frac{F(t)E^{*2}}{R^2} \right)^{\frac{1}{3}} \quad (6)$$

Using this maximum pressure p_0 at timestep t , we create the radial pressure field of contact $p(r, t)$. This expression comes directly from Hertzian contact theory [52].

$$p(r, t) = p_0(t) \sqrt{1 - \frac{r^2}{a^2(t)}} \quad (7)$$

Now, we will apply the method of dimensionality reduction (MDR). This technique is used to solve the stress field for surface deformation based on the assumption that contact geometries are axisymmetric. By utilizing this method, we are able to reconstruct the deformation of the sensor surface. We begin by transforming coordinates of the pressure field into one-dimensional force density q_{1D} through Eq. 8.

$$q_{1D}(x, t) = 2 \int_x^\infty \frac{rp(r, t)}{\sqrt{r^2 - x^2}} dr \quad (8)$$

From here, we apply a constitutive relationship on the sensor gel pad to get a one-dimensional displacement of the gel surface u_{1D} . This displacement is defined in the normal direction \hat{z} . By transforming to a single dimension, we restrict the displacement geometry to be axisymmetric about \hat{z} from the center $x = 0$.

$$u_{1D}(x, t) = \left(\frac{1 - \nu_{\text{sensor}}^2}{E_{\text{sensor}}} \right) q_{1D}(x, t) \quad (9)$$

The maximum displacement will occur at $x = 0$. We define this to be equivalent to our maximum measured depth d .

$$u_{1D}(0, t) = d(t) = \left(\frac{1 - \nu_{\text{sensor}}^2}{E_{\text{sensor}}} \right) q_{1D}(0, t) \quad (10)$$

Then, by plugging in $x = 0$, the expression for q_{1D} simplifies considerably.

$$u_{1D}(0, t) = d(t) = 2 \left(\frac{1 - \nu_{\text{sensor}}^2}{E_{\text{sensor}}} \right) \int_0^{a(t)} p(r, t) dr \quad (11)$$

We solve this integral to get Eq. 13 which expresses maximum observed surface displacement d in terms of normal force F .

$$\int_0^{a(t)} p_0(t) \sqrt{1 - \frac{r^2}{a^2(t)}} dr = \frac{\pi}{4} p_0(t) a(t) = \left(\frac{3F(t)E^{*2}}{32R^2} \right)^{\frac{1}{3}} a(t) \quad (12)$$

$$u_{1D}(0, t) = d(t) = \frac{1 - \nu_{\text{sensor}}^2}{E_{\text{sensor}}} \left(\frac{3E^{*2}F(t)}{32R^2(t)} \right)^{\frac{1}{3}} a(t) \quad (13)$$

We apply this relation for every timestep t over the duration of a grasp. Using all measurements of d , a , and F , we can apply a linear least-squares algorithm to retrieve a best fit value \hat{E}^* . Then, this estimate is used with known mechanical properties of our sensor’s silicone gel pads to compute the Young’s modulus of the unknown grasped object \hat{E}_{hertz} , as shown in Eq. 5.

Without the MDR, we could not have solved directly for the deformation of the gel surface, meaning we could not create an expression relating F directly to d in terms of Young’s modulus. Instead, we could only derive a relation for the apparent deformation of both bodies with respect to each other. This apparent deformation is equal to the displacement between both bodies, or change in gripper width Δw in our case. This is a classic tabulated solution for Hertzian contact between a sphere and a plane [52], written as Eq. 14.

$$F(t) = 2E^* a(t) \Delta w(t) \quad (14)$$

Notably, this model would not make use of tactile depth d and relies solely on gripper width w measurements. These gripper measurements exhibit a larger observed error than tactile depth measurements, which are higher-resolution and demonstrate sub-millimeter accuracy. For these reasons, we opt to use the MDR-derived solution.

B Markers

Markers are small black dots painted in an array on the surface of the GelSight gel pad. As the surface of the gel deforms and stretches, these markers move. Thus, we can track their relative position to map the displacement of the gel pad surface in both shear and normal directions. Markers have been shown to be effective for measuring shear and normal forces from tactile images [15, 22]. From a broad standpoint, this means we can use markers to increase the amount of dynamic information encoded in a tactile image. Without them, we could not estimate shear force.

In our experiment, we have created one GelSight Wedge [22] with markers painted on the surface. This was done to investigate how beneficial markers may be for estimating a dynamic property of contact like Young’s modulus. The difference between tactile images with or without markers for two objects is tabulated in Fig. 11. These markers help track surface displacement, but they may occlude fine features of texture, like screw threads.

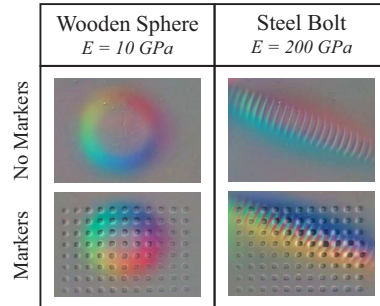


Figure 11: **Markers.** Tactile images from GelSight Wedge’s with and without markers. Tactile images are size 35mm by 25mm.

C Processing Grasp Data

We collect data over a set number of automated parallel grasps for every object in our dataset. Normal force F , width w , and maximum depth d are plotted for an example grasp of a rigid sphere in Fig. 12a. Grasps are executed at nearly constant velocity to a peak force of approximately 30 N. These measurements are clipped to the loading sequence based on force thresholding. Once force passes an empirically-defined threshold of 0.75 N, we consider the object to be in-contact with the

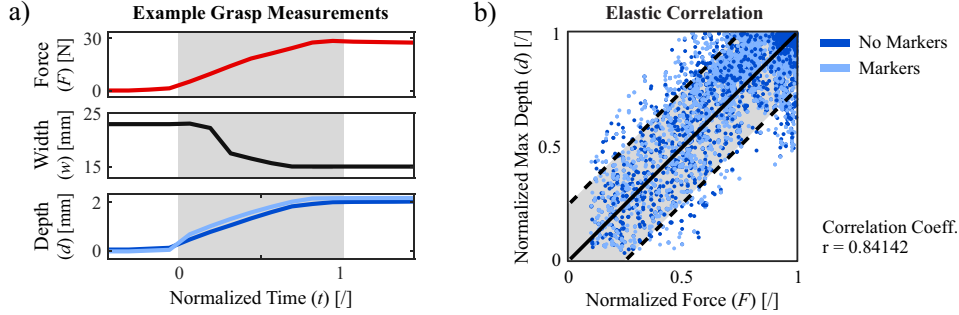


Figure 12: **Grasping data.** (a) Grasp data is plotted for an example grasp of a rigid sphere. The chosen loading sequence from initial contact to peak force is highlighted in gray. (b) Normalized force and depth measurements from all collected grasps are plotted. The correlation coefficient between these measurements is computed as 0.84 and bounds are placed at 25% error mark.

GelSight sensor and define this as timestep $t = 0$. We clip data from this point until the peak recorded force is reached.

As expected in an elastic regime, we observe that force and depth measurements are highly correlated from both GelSight sensors. Raw collected data normalized per grasp is plotted in Fig. 12b. Measurements are normalized according to their peak value over each respective grasp. These measurements are randomly sampled from grasps across the entire dataset. All measurements outside of 25% correlation bounds are discarded. Over 90% of measured points lie within these bounds for both sensors. We observe that there is no distinguishable difference between measurements collected from one sensor to the other.

D Dataset Diversity & Performance

The diversity of the collected dataset is characterized through categories of material and shape in Tables 2 and 3. As intended, the most common material of objects in the dataset is rubber, which includes 28.6% of the objects in the dataset. This is done to bias the dataset toward the Young’s modulus of our sensor’s gel pads. There are significant percentages of metal and plastic objects, making up 25.1% and 24.0% of the dataset respectively. Over 50% of objects in the dataset have irregular shapes. This is done to diversify training data in an attempt to learn Young’s modulus independent of object shape or contact profile. Still, there are substantial percentages of simple shapes for performance evaluation.

Table 2: Dataset Material Distributions

Material	Percent (%)
Rubber	28.6%
Metal	25.1%
Plastic	24.0%
Wood	8.4%
Foam	6.3%
Other	7.6%

Table 3: Dataset Shape Distributions

Shape	Percent (%)
Cylinder	20.2%
Sphere	11.5%
Rectangular	15.3%
Hexagonal	2.1%
Irregular	50.9%

Results of investigated methods on unseen objects across shape and material categories are compared in Fig. 13. We observe that neural network methods give the lowest log10 error and accuracy in nearly every category. Moreover, the accuracy increases and error decreases with the complexity of analytical models. Our Hertzian method performs best over spheres, which is expected given that this model assumes spherical contact geometry. Most critically, it is shown that our trained model can learn Young’s modulus independent of shape, given that prediction accuracy and error remain consistent across different object shapes. The model performs robustly across different categories of materials as well.

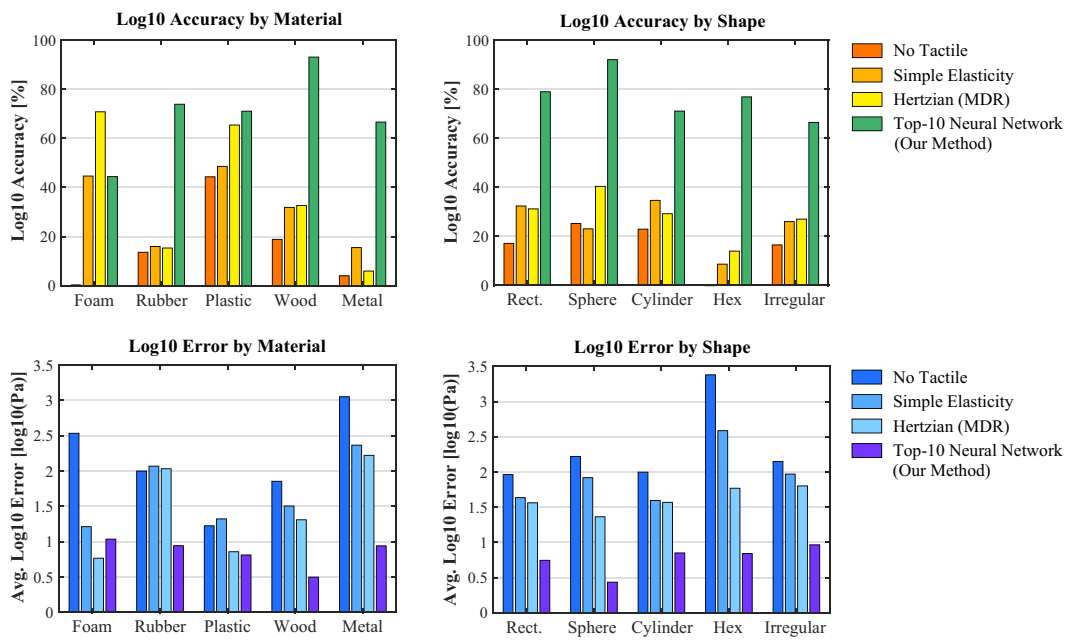


Figure 13: **Estimation methods performance.** Log10 error and accuracy are plotted for each estimation method across dataset categories of shape and material. Neural network results are from top-10 trained models evaluated on unseen objects.